

Observed non-linearity of Darcy-permeability in compacted fine pigment structures

Joachim Schoelkopf*, Patrick A.C. Gane and Cathy J. Ridgway

Omya AG, CH 4665 Oftringen, Switzerland

* Corresponding author. Fax: +41 62 789 2397 Tel.: +41 62 789 2229 E-mail address:

joachim.schoelkopf@omya.com

Abstract

Liquid permeability was measured on a range of porous samples, using a specially-constructed high pressure permeation cell. The samples consisted of compacted fine isotropic mineral pigment - calcium carbonate - compressed over a range of compaction pressures. These samples have pore diameters typically (number basis) finer than 0.1 μm . The porosities and the pore size distributions of the samples have been determined by means of mercury porosimetry.

The permeability of these fine-pore network systems is seen under certain conditions not to obey the well-known linearity of the Darcy relation as a function of applied liquid pressure differential. A considerable pressure-flux hysteresis is observed following saturation by imbibition. Furthermore, it is seen that there is no direct linear correlation between permeability and porosity despite the use of a constant pigment particle size distribution and, hence, skeletal size distribution. The measured permeability displays a local maximum at a fractional porosity of approximately 0.26 with a further distinct drop at around 0.27. Interestingly, this phenomenon is also confirmed using a computer-based porous network simulator which provides a relative permeability based on matching the mercury percolation data.

Taking into account the effects of earlier-proposed mechanisms of preferred pathway flow and film flow during imbibition, it is postulated that some pores remain unfilled during imbibition and saturation prior to the permeability study, such that there remains entrapped air or vapour phase in microscopic ganglia. This air does not dissolve in the aliphatic mineral oil used in the experiments. Structures with a delineated pore-throat structure will probably lead generally to observed non-linear phenomena within the range of dimensions studied here, which can have implications, amongst others, for microscopic filtration, catalysis and absorption phenomena.

Keywords: liquid permeability, Darcy permeability, network simulator, pore structure, porosity, permeability hysteresis

1. Introduction

Permeability defines quantitatively the extent to which a porous material allows a fluid to pass through under a given pressure differential. In this sense a lot of parallels can be seen with the physics of electrical conductivity or its inverse, electrical resistance. In the same way, non-linearity in permeability can have its parallels with inductance and capacitance. Absolute permeability covers one phase flow through a saturated sample, relative permeability is linked to multiple phases and their distribution characteristics within the porous network. Permeability issues are important to many different industries and much work has been carried out in the petroleum industry, agriculture and soil science, pharmacology, textile research and to a lesser extent in the paper industry.

This study was instigated by the paper industry where a transplanar permeability value is practically desirable and is usually obtained by pressure driven air permeation through a paper sheet. Although this method is widely used, the major drawbacks are that the transplanar flow, defined as the z direction through the sheet, is only through one sheet of paper, so even one pinhole will strongly influence the result. Also, the fluid used (air) is highly compressible and the sealing of the area to be measured is not trivial. A method has therefore been developed for the studies reported here to overcome these drawbacks by using an incompressible fluid, i.e. liquid (mineral oil), that does not cause swelling or de-hydrogen-bonding of the fibres. The method has been applied to samples consisting of a pile of 1.5 cm side length squares of paper which are firmly embedded in a resin around their edges (more than 120 individual sheets are used) [1].

Previously attempts have been made to link uni-directional permeability (z direction) directly with isometrically averaged porosity, as measured, for example, by oil saturation or mercury porosimetry. However, this is problematic. Paper is produced not only as a sheet-like formation but also under conditions of shear in the direction of the paper machine. This induces a strong directionality in the xy plane, following the machine direction. A paper structure is therefore similar in some ways to a mesophase crystal (liquid crystal) in that fibres become aligned in two dimensions. When the paper is coated, the structures formed are then not only directional but also layered.

Today, most added value papers are covered with coating that contains mainly mineralic pigments and organic binders. Coatings are applied to paper to achieve uniformity of surface for printing inks, lacquers, and the like, to obtain printed images without blemishes visible to the eye. Furthermore, they enhance opacity, smoothness and gloss (or evenness of matt finish) of paper or paperboard. The upgrading effect of coating on basepaper stock in respect to weight and composition also makes it more economical.

The method developed and used in this work focuses on the paper coating pigments. Instead of using coated layers we chose to involve macroscopic blocks of mineral coating pigments, namely fine ground Calcite, CaCO_3 , as model structures for paper coatings. Using a compact formation technique applying different compaction pressures in a tablet press, a wide range of porosities and mean pore diameters were achieved without changing the surface chemistry or intrinsic pore geometry of the structures. This range of structures is seen to contribute a

unique series to the literature upon which consistent studies of mercury intrusion/extrusion, imbibition and permeation can be made.

The absolute liquid permeabilities of the samples were measured using a specially designed pressure-driven permeameter. The measured liquid permeabilities were then compared with those predicted by the network simulator, Pore-Cor¹, providing for the first time a direct experimental challenge to the permeability simulation algorithm of the model published by Matthews *et al.* [2].

The method developed and introduced here is suitable for a multitude of macroscopic materials. The preferential form is a cuboid sample such as consolidated pigment tablets, semi-friable porous media and multi-layers of planar substrates. As an example of the latter case, this method removes the major uncertainties involved when measuring the permeability of a small area of a single inhomogeneous sheet of paper. However, it requires very careful sample preparation and handling, and the experiment itself takes considerably longer than the standard methods.

2. Theory

We briefly look at permeation, which is the motion of a liquid flowing through a porous substrate without a specification of an internal driving force. It is mostly defined for an external pressure-driven process in an effectively saturated sample. Hilfer [3] states that the permeability is the most important physical property of a porous medium in much the same way as porosity is its most important geometrical property. The permeability K is expressed using Darcy's Law [4] Eq. (1),

$$q = \frac{r^2 A \Delta P}{8\eta l} = K \frac{A \Delta P}{\eta l} \quad (1)$$

balancing the driving pressure ΔP with the viscous drag derived from the Poiseuille equation, Eq. (2)

$$q = \frac{\pi r^4 \Delta P}{8\eta l} \quad (2)$$

where q is the volumetric flow rate, r is the radius of the circular tube assumed in the Poiseuille analysis representing the equivalent flow dimension of a unit cross-sectional area of the sample, η is the fluid viscosity, A the total sample cross-sectional area and l its length.

Darcy pioneered the topic of permeability, formulating the classical relationship given in Eq. (1). This equation has been widely adopted, has been adapted to more complex situations and has also been related to further

¹ Pore-Cor is a software package developed by the Environmental and Fluid Modelling Group, University of Plymouth, Devon PL4 8AA, U.K.

structure parameters. Among the more popular extensions is the Carman-Kozeny approach [5], often called the "hydraulic radius theory", linking the void volume in a porous medium, ϕ , with its inner specific surface area, s ,

$$r_h = \frac{\phi}{s(1-\phi)} \quad (3)$$

[6], where r_h is the hydraulic radius, and

$$K = \xi \frac{\rho g}{\eta} \frac{\phi^3}{\tau^2 (1-\phi)^2 s^2} \quad (4)$$

[6], where ξ is a function of the tube cross-sectional shape, (for cylinders $\xi = 0.5$), ρ is the density of the fluid, g is the acceleration due to gravity, associated with an assumed vertical flow, and τ stands for a tortuosity term

$$\tau = l_e / l \quad (5)$$

where l_e represents the effective path length through a sample. For details and variations, the reviews of van Brakel [6] and Dullien [7] give further insight.

In soil and petroleum science, K is often employed in the form of a permeability tensor to describe the permeation characteristics in a spatial (mostly macroscopic) context. Relative permeability is also used to describe permeation as a function of saturation with a third phase.

The permeability of a growing filtercake of paper coating particles was recently reported by Lohmander *et al* [8]. Much similar work has been carried out considering fibres, as the permeability response of a forming fibre mat is naturally the basis of paper making.

The limits of the Darcy regime have also been analysed. They can be exceeded by the presence of turbulent flow, liquid circulating in pores (pore-level eddies), entrapped ganglia of a different phase in small capillary features, which may start to move at a pressure threshold value and at very low flow rates where interactions between the fluid and the pore walls become influential, [3,9-11].

2.1 The computer network model and permeability algorithm

The experimental data in this work are compared to Pore-Cor which is a computer network model simulating the void-space structure of porous materials based on an array of pores and connecting throats. It has been used to simulate the structures of a wide range of porous materials including sandstones [2], paper coatings [12], medicinal tablets [13], and soil [14]. The unit cell consists of 1 000 cubic pores in a 10x10x10 array, connected by up to 3 000 cylindrical or double conical [18] throats, i.e. up to one connected to each cube face depending on the connectivity (average number of throats connecting to each pore in the unit cell). The centre of each pore is equally spaced from its neighbouring pores by the 'pore row spacing' Q , and each unit cell is therefore a cube of side length $10 Q$. Periodic boundary conditions are applied, i.e. each cell is connected to another identical unit

cell in each direction. Connectivity, and therefore flow, is maintained between adjacent unit cells in the x , y , and z directions. When attempting to model real systems, the pore- and throat-size distribution of the unit cell is optimised so that the simulated percolation curve fits as closely as possible to the corrected experimental mercury intrusion curve [15]. The pore and throat size distribution is characterised by two parameters, 'throat skew' and 'pore skew'. The distribution of throat sizes is chosen to be log-linear, i.e. there is an equal number of each logarithmic size step, and since there are 100 such steps, the distribution line before the application of the skew parameter is given by 1 % of each size. The "throat skew" is the percentage number of throats of the smallest size, i.e. the percent of smallest throats is given by "throat skew" %. The throat skew parameter acts to pivot the size distribution about its mid-point, raising the number of fine throats above 1 % and lowering the number of largest throats accordingly below 1 %. The pore size is determined as the size of the largest throat connecting to that pore. The "pore skew" increases the sizes of the pores by a constant multiple, used to aid the fit to the overall void size distribution from mercury intrusion. However, the pores with the largest sizes are truncated back to the size of the largest throat to avoid distortion of the model lattice, thus giving a peak in the distribution at the maximum size.

The positions of the pores and throats are random, being determined by a pseudo-random number generator. The percolation characteristics of the network are insensitive to Q . Therefore, after convergence of the simulated percolation to the experimental percolation has been achieved by scanning through values of throat skew and connectivity, Q is adjusted so that the porosity matches the experimental value while ensuring that no pores overlap. The connectivity and throat skew parameters are therefore somewhat arbitrary fitting parameters giving useful information about the model structures, but, since they are not independently determined without reference to the pore parameters, they do not give a direct physical characterisation.

It has been found that it is not normally possible to represent the overall complexity of the void network of a natural sample using the relatively simple geometry of a single unit cell. The size of the unit cell is often smaller than the representative elementary volume (REV) of the sample. Therefore, different unit cells must be generated using a different seed for the pseudo-random number generator. The model is designed so that different structural parameters in conjunction with the same seed of the pseudo-random number generator produce a family of unit cells which are similar to each other – for example, all may have a group of large pores in the same region. This aspect of the modelling is discussed in detail [14]. Different stochastic generations use a different pseudo-random number generator seed, and can either use the original optimisation parameters or can be re-optimised to the experimental data. The parameters and procedure are described in detail in previous publications [13,16]. Recent developments to the network simulator include an imbibition algorithm [12,17-20] based on Bosanquet's equation [21], the introduction of bi-conical throats [20] and the ability to produce non-isotropic structures [22]. An improved permeability algorithm was recently introduced [23] and is summed up in the following.

In the Poiseuille equation, Eq. (2), the term r^4/l corresponds to the volumetric flow capacity $\bar{\mathcal{E}}$. In using this equation, it should be recognised that it is only a first approximation to the resistive flow of a feature within the network.

It is assumed that Poiseuillian flow occurs across the whole cell:

$$\left(\frac{dV}{dt}\right)_{\text{cell}} = -\frac{\pi}{8\eta} \Omega_{\text{cell}}(\mathcal{E}_{\text{arcs}}) \Delta P_{\text{cell}} \quad (6)$$

where Ω_{cell} is an averaging operator over the whole unit cell, operating on the flow capacities of the arcs ($\mathcal{E}_{\text{arcs}}$).

An arc represents a pore-throat-pore pathway and a node is the centre point of each pore [2]. Each arc in the flow network is the flow channel between adjacent nodes. Again, there is an approximation in doing this. The model implicitly assumes that Poiseuillian flow occurs at all points within the network. It ignores non-Poiseuillian flow that occurs at corners and other feature discontinuities [24]. The algorithm generates a term which is related to the effective Poiseuillian capacity of the cell for flow in the $-z$ direction (from the top to the bottom face), and in the $\pm x$ and $\pm y$ directions. Flow, however, is not allowed in the $+z$ direction, thereby applying an implicit positive pressure gradient with respect to z . The combination of Eq (1) and Eq. (2), results in an expression for the absolute simulated permeability independent of the pressure gradient imposed on the sample:

$$K_{\text{sim}} = \frac{\pi}{8} \Omega_{\text{cell}}(\mathcal{E}_{\text{arcs}}) \frac{l_{\text{cell}}}{A_{\text{cell}}} \quad (7)$$

A network analysis approach to this problem supplies a term $\Omega_{\text{cell}}(\mathcal{E}_{\text{arcs}})$ as the maximal flow capacity through the network of pores and throats. It is calculated by means of the ‘Dinic’ network analysis algorithm [2]. There is an overall conservation of flow, so that the entire volume of fluid entering the top of the unit cell emerges at the bottom, with no build-up through the network. The value obtained, as the maximal flow, is an average of the capacity values over only the channels found to carry flow.

3. Experimental method and materials

An experimental sample preparation method was previously developed in which consolidated pigment structures are formed [25]. By applying different compaction pressures, a wide range of usable porosities can be obtained from a single consistent powder material which can be well characterised using mercury porosimetry. The key point is that without changing the surface chemistry or intrinsic skeletal geometry, a range of usable porosities and d_{50} pore diameters can be achieved (d_{50} is the Laplace diameter at 50 % intrusion volume of the mercury intrusion curve).

3.1 Calculation of required liquid permeation pressures

To use this work for comparisons in the wider context of the impact of permeability on absorption dynamic [26], the measurement of the absolute liquid permeability must be made using a constant differential pressure which is (i) of a magnitude which moves the fluid through the structure at a rate regime similar to that experienced during imbibition [27], while (ii) generating a steady state flow regime on a sample scale which is laminar rather than

turbulent, so that Darcy's law is valid. Condition (ii) may follow naturally from condition (i), however calculations are carried out for both conditions to check that the flow is in the correct regime.

i) During imbibition, the driving force is the pressure differential across the liquid menisci, which is acting against the viscous and inertial drag of the liquid. The movement of the wetting front becomes slower as the viscous drag in the system increases (hence the \sqrt{t} relationship for longer imbibition times). The viscous forces during the measurement of absolute liquid permeability approximately correspond to the imbibition conditions at $t = \infty$, when the viscous drag is at a maximum. Since the liquid is moving at a constant rate during the permeability experiment, the inertial forces, so prevalent in respect to imbibition, can be taken as negligible. During the measurement of permeability, the sample is essentially full of liquid, (apart from very small pockets of trapped gas/air as discussed later). Therefore, there are no menisci driving the liquid and so inertial wetting can be eliminated. Instead, the external applied pressure drives the fluid. In imbibition, however, it is the resultant of the viscous, inertial and capillary forces that cause the fluid to move through the structure. A similar rate of movement during the permeability experiment must be achieved by a balance between the viscous forces and the external pressure only. Therefore, the external pressure to achieve usable fluid flow rates can be approximated as being the same as the capillary pressures during imbibition. Using the Laplace equation, Eq. (8),

$$\Delta P = \rho gh = \frac{2\gamma \cos \theta}{r} \quad (8)$$

the pressure was computed from the surface tension of the mineral oil used, "PKWF 6/9 af neu", (af 6/9), Table 2, having a contact angle of 0° (assuming complete wetting) and a typical throat radius of 100 nm. A value of $\approx 548\,000$ Pa = 5.48 bar was obtained. Pressures in a range centred on this value should therefore cause fluid movement at rates comparable to those towards the end of the imbibition experiment.

(ii) The standard means of characterising the flow regime is by use of the Reynolds number, Re

$$Re = \frac{\rho v 2r}{\eta} \quad (9)$$

which balances inertial with viscous forces and indicates the onset of turbulent flow within the microscopic pore structure, where v is the velocity.

Again, since we want to relate the permeability flow rate to that of imbibition, the flow rate through a feature, p , within the void structure during permeation should be chosen to have a similar order of magnitude to the rate of movement of the entire average wetting front. The latter is expressed as a change in distance of the wetting front from the source, measured as a Darcy length, with time. As explained above, the limiting rate of movement as t approaches infinity needs to be considered.

An experimental value for the limiting rate of movement, expressed as a Darcy velocity, is:

$$v_p = \frac{dm}{dt} \frac{1}{\rho \phi A} \quad (10)$$

Taking values of density ρ and viscosity η for the mineral oil, and substituting them into the Reynolds equation for a pore [11] gives a relationship between the Reynolds number and the void feature radius, r_p :

$$Re_p = \frac{dm}{dt} \frac{2r_p}{\eta \phi A} \quad (11)$$

Solving Eq. (11) for dm/dt in order to reach Seguin's critical limit of laminar flow at $Re_p = 180$, mass flow rates of magnitude $\gg 1 \text{ kgs}^{-1}$ would be needed. Therefore, the experimentation with expected flow rates in the order of 0.0001 kgs^{-1} is certainly to be in the laminar regime of flow.

3.2 Construction of the pressure cell

The cell design used for the pressurised permeability experiments is shown in Fig. 1. The individual parts of the cell are machined from aluminium and connect via large pitch threads to enable complete and easy assembly/disassembly. The use of the resin to embed the cuboid porous pigment samples (see below) allows for rigid clamping and sealing of the sample into the pressure cell chamber. Gas over-pressure is supplied from a nitrogen bottle and passes a precision pressure reduction valve (Messer FM 62²). A Y-piece connects a digital barometer (Eurolec³ PR 205, 0 - 7 000 mbar) to the pressure line. This gauge was zeroed to atmospheric pressure daily, and therefore all pressures mentioned are gauge - i.e. differential pressures ΔP relative to one atmosphere. The pressure cell is fixed on a tripod over a micro balance. A PC samples the balance data using specially-developed software developed within Omya AG⁴. A drop captor device was needed in the base of the cell to guide the permeated liquid drops to the outlet. An important point of practical technique is that the whole chamber below the position of the sample has to be pre-wetted with the liquid so that each drop leaving the sample causes a drop to fall into the sampling dish. Once these precautions are taken the continuity of flow is ensured.

² Messer Griesheim GmbH, Füttingsweg 34, D-47805 Krefeld, Germany, worldwide see www.messergroup.com

³ Eurolec Instrumentation Ltd., Cluan Enda, Dundalk, Co. Louth, Eire

⁴ Software can be obtained on request from Dr. D. Spielmann, Omya AG Postfach 32, CH 4665 Oftringen, Switzerland

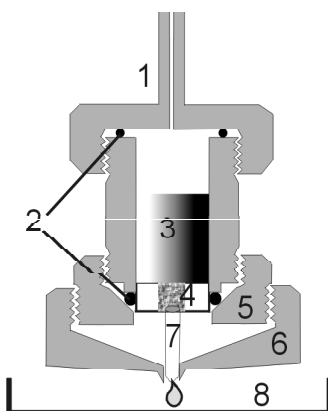


Fig. 1 Permeability measurement cell : (1) lid with pressure inlet, (2) sealing O-rings, (3) liquid cell; outer diameter = 40 mm, (4) porous sample embedded in resin disc of diameter = 30 mm, (5) fixing ring compresses the O-ring which seals the resin disc, (6) security shroud and drop collector, (7) drop captor (Teflon tubelet), (8) dish on micro-balance.

3.3 Embedding materials and sample preparation method

The epoxy resin was from Buehler Epothin⁵. The PTFE-moulds for the casting of the embedments from Prüfmaschinen AG⁶ are circular having an inner diameter of 30 mm.

The compressed tablet structures are ground into samples of cuboid shape (the grinding equipment has been described previously, [12]) which are placed into the moulds and the resin poured around them. The quickly rising viscosity of the chosen curing resin results in a penetration of approximately 1 mm locally at the outer boundaries of the sample. This penetration depth is clearly visible because of the opacity change at the edge of the sample and can, therefore, be calibrated. The open area of the porous sample, i.e. that free from resin, is evaluated so that the permeable cross-sectional area can be established. Subsequently, the sample discs are removed from the mould and dry ground on the two circular surfaces till the open porous structure is reached. Compressed air is carefully blown over the sample to remove any dust. Subsequently, the sample discs are placed in a dish containing the probe liquid in order to saturate the void network of the sample by imbibition before placing in the apparatus.

3.4 Sample structures and liquid used

Experimental porosimetry and simulated network model parameters of the experimental sample structures used in this study are given in Table 1, (for parameter definitions see section 2.1). The properties of the used mineral oil, af 6/9, are shown in Table 2. The oil consists of a fraction of aliphatic alkanes, free of aromatic components.

⁵ Epothin is a product name of Buehler Ltd., 41 Waukegan Road, Lake Bluff, IL 60044, USA

⁶ Prüfmaschinen AG, Giessenstr. 15 CH-8953 Dietikon, Switzerland

Per definition the surface tension of these alkanes is purely of the Lifshitz- van der Waals type, formerly called dispersive components.

Table 1 Pore-Cor parameters and simulated permeabilities for the structures used for permeability experimentation with oils.

Fractional porosity	Throat type	Pore skew	Throat skew	Connectivity	Pore row spacing, Q (μm)	K_{sim} (liquid) (mD)
0.2463	Cylindrical	1.4	0.99	3.4	1.73	4.45E-05
0.2634	Cylindrical	1.4	1.42	4.4	1.25	1.01E-04
0.2673	Cylindrical	1.1	0.87	3.4	1.23	1.44E-04
0.2704	Cylindrical	1.4	0.89	3.3	1.36	9.56E-05
0.3307	Cylindrical	1.2	0.60	3.3	1.25	6.20E-04
0.2463	Conical	1	0.12	2.6	1.47	8.96E-04
0.2634	Conical	1	0.14	3.2	1.62	1.67E-03
0.2673	Conical	1	-0.03	2.7	1.46	1.21E-03
0.2704	Conical	1	0.01	2.8	1.47	8.92E-04
0.3307	Conical	1	-0.26	2.9	1.35	3.60E-03

Table 2 Liquid properties of mineral oil

	Viscosity ($\text{Pa s} \times 10^{-3}$)	Surface tension ($\text{Nm}^{-1} \times 10^{-3}$)	Density ($\text{gm}^{-3} \times 10^6$)	Boiling point ($^{\circ}\text{C}$)
PKWF 6/9 af neu	4.3	27.4	0.805	160 - 290

4. Results and discussion

The first results showed an unexpected behaviour in that the flux at a constant pressure did not appear to be constant with time. An extreme example showed no flow at 3 bar differential pressure, but significant flow when the differential pressure was increased to 7 bar, which then continued proportionally reducing when the pressure was again lowered to 3 bar. Examples of less extreme behaviour are shown in the graphs in Fig. 2. However, this behaviour was seen to be arbitrary on more than 10 different samples investigated. It was not possible to see a breakthrough correlation as a function of time or porosity suggesting a compressive component or application of the percolation

theory.

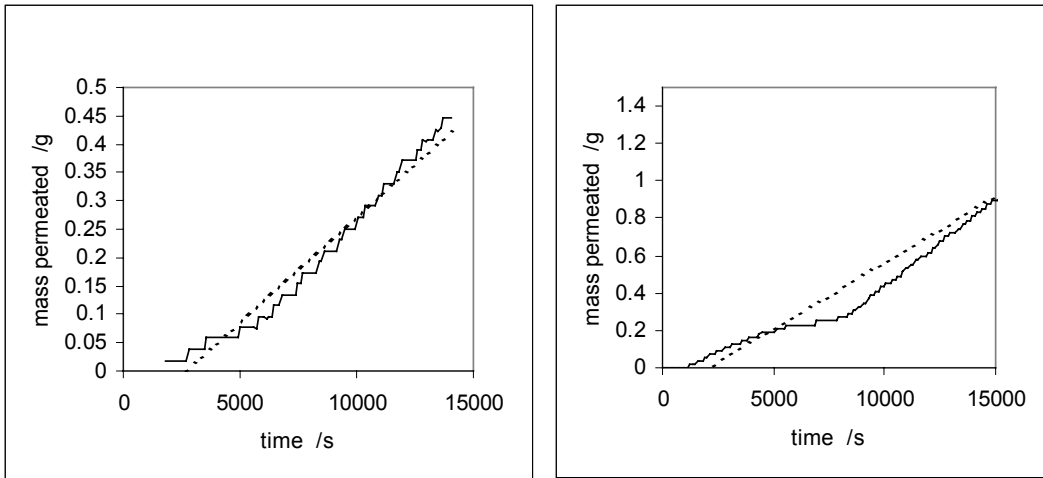


Fig. 2 Non- linear flow at constant pressure, left: 7.22 bar, 0.2302 fractional porosity, right: 5.10 bar, 0.2463 fractional porosity.

It was suspected that entrapped air bubbles could be the cause. If they start to move or become compressed, constant flow can only be achieved when the air is displaced or moved into stable trapping positions consistent with the applied pressure and resulting flow. In order to investigate this issue further a hysteresis experiment was performed.

The sample was handled with the utmost care, making sure that no air could be introduced and trapped during the sample saturation or during the mounting into the measurement cell. A pressure hysteresis loop was then recorded as shown in Fig. 3. The individual points show an average flow at a constant pressure over an extended period of time $t > 10^4$ s.

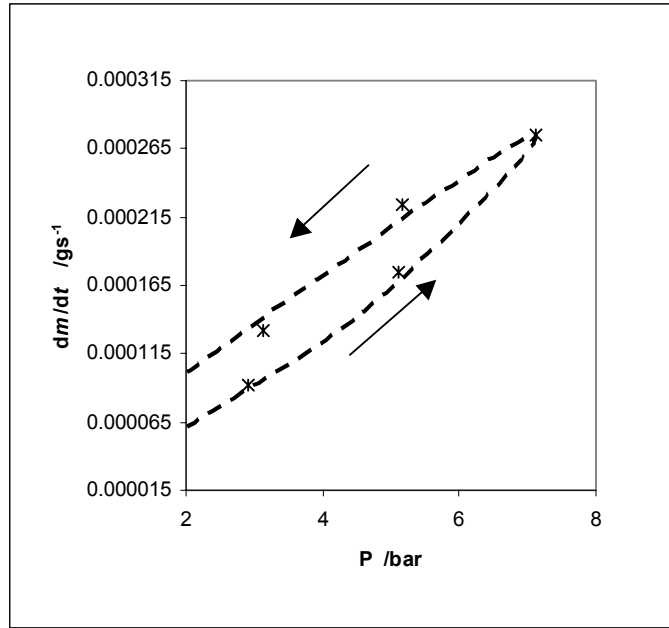


Fig. 3 Hysteresis of flow as a function of pressure: 0.3298 fractional porosity.

Clearly, the dependence of flow on sample pressure history (applied differential pressure) is evident. Once again, the flux is dependent on the starting pressure. If the effect would be due to pore-scale eddies or similar phenomena, hysteresis would not necessarily be expected. So, the previous assumption of trapped air bubbles, which at a given pressure threshold value may start to move and are partly extruded, seems to be the most likely answer. The measurement routine above, starting with the highest pressure first, ensured, at least, that there was no further bubble motion at lower pressures, but the amount of remaining entrapped air is not yet known. It has to be further assumed that the entrapped vapour bubbles do not occur during the sample handling after the supersource soaking, but during the supersource imbibition itself.

Cycles of measurements were thus performed, first with the highest possible pressure (≈ 7 bar) and then recorded in descending order of pressure. A decreasing series of pressure steps are used to record the permeation flow over a reasonable amount of time to achieve a plot with a usable gradient. Such an experimental data set is shown in Fig. 4. Each step in the recorded curve is caused by one drop falling into the weighing pan. By making a linear regression analysis using Microsoft Excel, a gradient is determined which represents a flow rate of mass per unit time. It is clearly visible that the flow is in the necessary steady state at a constant pressure.

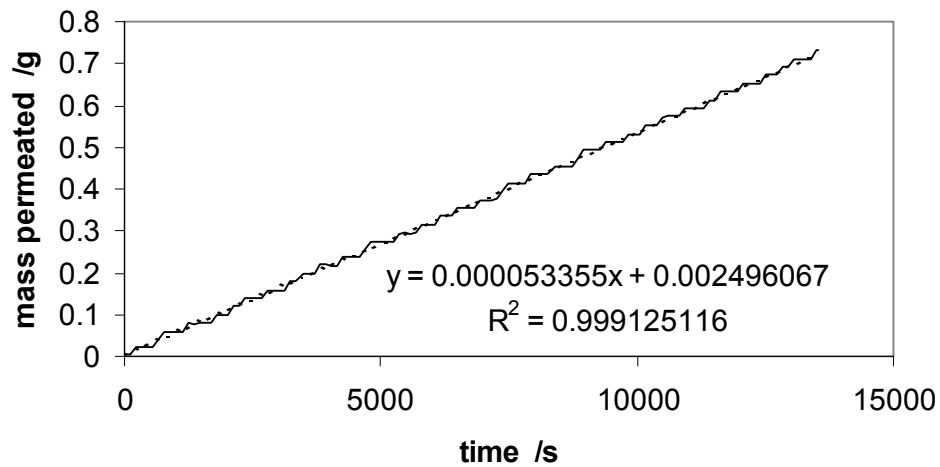


Fig. 4 Typical permeation curve, 0.2634 fractional porosity, $P=4.82$ bar.

Determining gradients of further samples in this manner gave the initial data in Fig. 5 and for a more extended range of porosities in Fig. 6. Although these plots look reasonable in terms of pressure / flow rate ratios and seem also to track with the porosities, they do not yet contain the sample size parameters needed to derive a permeability.

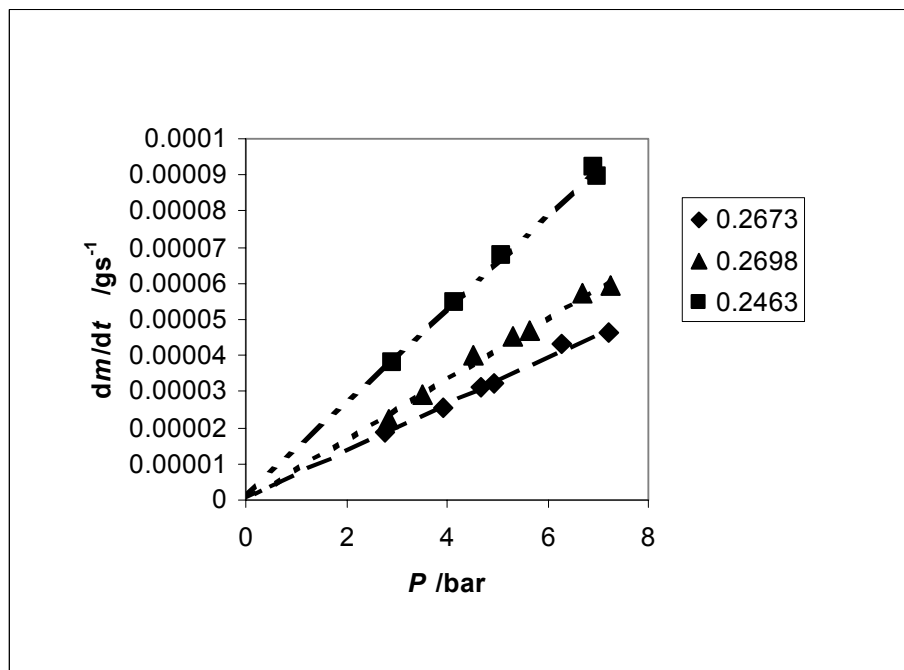


Fig. 5 Permeation gradients in a single sample as a function of applied pressure (legend shows fractional porosities as measured by mercury porosimetry).

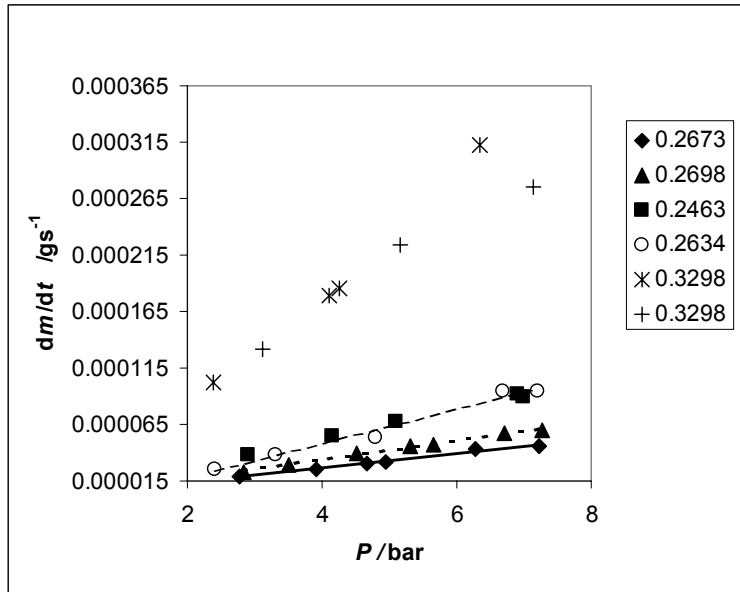


Fig. 6 Permeation gradients in a single sample as a function of applied pressure (legend shows fractional porosities as measured by mercury porosimetry).

As soon as an "equivalent hydraulic capillary" radius r_{ehcDarcy} is calculated by solving Eq. (1) where the term r is now r_{ehcDarcy} and inputting the necessary dimensions of the sample, r_{ehcDarcy} falls out of correlation with porosity, Fig. 7. The consequence is that porosity in these samples seems not to be the linear controlling factor of permeability.

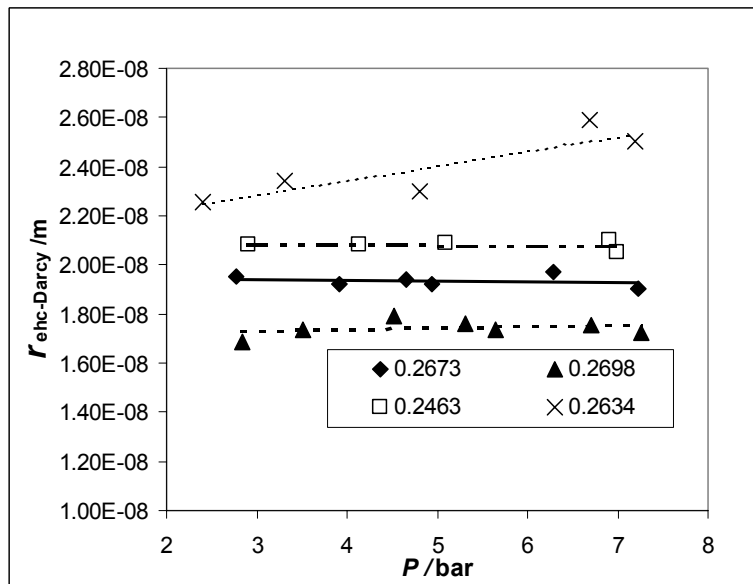


Fig. 7 Hydraulic radii not tracking with porosities (legend shows fractional porosities as measured by mercury porosimetry).

4.1 Theory of entrapped micro-bubbles

The finding that imbibition saturation leaves the sample with some entrapped air is in contrast to earlier statements, where it is described that a range of different liquids under supersource conditions imbibe into the whole pore structure present as determined by independent methods, i.e. by mercury porosimetry and Archimedes calculations [25]. How can these apparent contradictions be explained, and can they contribute to a better understanding of flow mechanisms?

Assume the dimensions of one of the porous pigment samples has a cross-sectional area of 1 cm^2 and a volume of 1 cm^3 . It is known that the skeletal particles are in an average size range of $1 \text{ }\mu\text{m}$. It follows that a row of 10 000 particles can line up along the sample edge, and in one in-planar layer of, say, cubic packing there are 10^8 particles. Assume there is 1 pore between 2 particles and omit the boundary zones in order to get a rough estimate of 99 960 000 pores per layer and therefore 9.99×10^{11} pores in the sample. Suppose a mean pore size is such that a spherical bubble fits into it with a diameter of $0.2 \text{ }\mu\text{m}$. (This would be the case for particles with a radius of $1 \text{ }\mu\text{m}$ in tetrahedral packing, [28,29], for finer particles the argument for this bubble size would be even stronger.) Such a bubble has a volume of $0.00418 \text{ }\mu\text{m}^3$. So if one planar layer of pores is completely blocked by entrapped bubbles, the summation of the bubbles' volume is $418\,432.56 \text{ }\mu\text{m}^3$. This is equivalent to a mass of 0.3368 ng of displaced liquid as calculated using the mineral oil at $6/9$ ($\rho = 805 \text{ kgm}^{-3}$), which is far less than a microbalance can detect. Therefore, even with millions of entrapped bubbles in a sample they cannot be gravimetrically detected. So although the sample saturates as well as a sensitive balance can determine, there may well be a significant number of pores remaining that contain vapour.

According to the size of an individual bubble, and the size and geometry of its host void, there are two distinct types of behaviour. The extreme behaviour mentioned above can be attributed to air bubbles which move and are flushed from the sample under pressure. The less extreme behaviour is due to air bubbles which move slightly or merely compress under increased pressure. The effect on permeability caused by both types of behaviour decreases with pressure, as compensated for in the experimental procedure.

The preferential wetting pathways during imbibition, as described in detail in previous work [12,18,20] are likely to cause the formation of the bubbles, since wetting through fast pathways overtakes that in slow pathways, and the exit route of air from the slow pathway is potentially cut off, thus producing a trapped bubble.

Linked to this potential effect is the evidence of adsorbed layers of water on the inner surface of the porous network and the known phenomenon of capillary condensation. This results in micro-pores filled by water which is also not soluble in the mineral oil and may block the relevant ganglia. As this effect is expected only in micro-pores it presumably does not influence the permeation behaviour significantly, which is determined mostly by pathways of interconnected large voids. It can also therefore be surmised that the entrapped air is associated with larger voids since it impacts on the permeability.

4.2 Comparison of experimental and modelled permeabilities

Fig. 8 shows the measured liquid permeabilities as a function of the porosity of each sample. It can be seen that there is a discontinuity in the permeability trend - i.e. the trend of increasing liquid permeability as a function of porosity unexpectedly reverses between the porosity data points of 0.2634 and 0.2704. This accounts for the non-linear response of the r_{heDarcy} against pressure plots to porosity shown in Fig. 7. The graph also shows the error bars which correspond to the scatter in behaviour from a straightforward Darcy proportionality of flow to differential pressure. This scatter is partly experimental, and partly attributable to entrapped bubbles as discussed earlier. It can be seen that despite these uncertainties the overall trend and its discontinuity are significant.

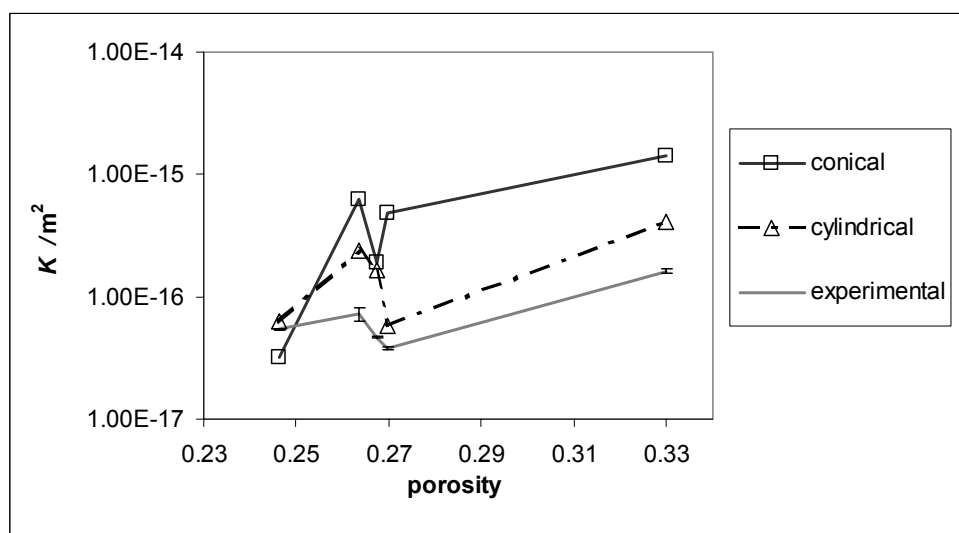


Fig. 8 Experimental permeability K calculated using Eq. (1) as function of fractional porosity. The error bars indicate the variation under different experimental pressures as shown in Fig. 7. Comparison is given to two different network simulations involving conical and cylindrical throats. (Note: 1 Darcy is equal to $0.987 \mu\text{m}^2$).

Also shown on the graph are the liquid permeabilities predicted by the network simulator. It can be seen that the simulated structures with cylindrical throats give a close match to the trends. However, the structures with cylindrical throats cannot achieve the correct porosity without invoking a rather arbitrary bulking up of the pore sizes, using the parameter known as 'pore skew'. The conical throat structures, by contrast, generate a higher porosity without requiring this bulking up. The conical throat structures are therefore generally more qualitatively realistic, although their absolute values are less representative. Entrapment during imbibition is facilitated by a delineated pore-throat structure. Structures without a delineated pore-throat structure will also probably lead to an easier and complete extrusion of bubbles. Experiments, for example, with uncoated paper samples as embedded porous material, yielded good consistent results, showing no hysteresis, [1].

The matching of the simulated and experimental trends allows one to go a step further and to use the simulation to explain the discontinuity in the permeability trend. Analysing the parameters of the computer network simulator it is found that there is no obvious discontinuity in the single reported parameters - it looks as if a combination of the throat skew (throat sizes) and connectivity contributes to the "dip" in the curve. This

combination of parameters could possibly be explained by conformal changes in the compacting of the particles, as mentioned by Toivakka and Nyfors [30], who found connectivities up to 9 for some packing modes. Another explanation could be that under the inter-particle stresses during compaction break up of agglomerates takes place. In the agglomerated state, the interstitial voids are smaller than in the de-agglomerated stage, but the voids between the agglomerates are larger. Hence, the permeability of an agglomerated sample may be larger than the one of an unagglomerated sample although the porosity will be reversed. Both proposals lead to temporarily larger voids in the structure, thus influencing permeability. The unit cells of the samples modelled by both conical and cylindrical throats at the critical porosities of 0.2634 and 0.2704, respectively, are shown in Fig. 9.

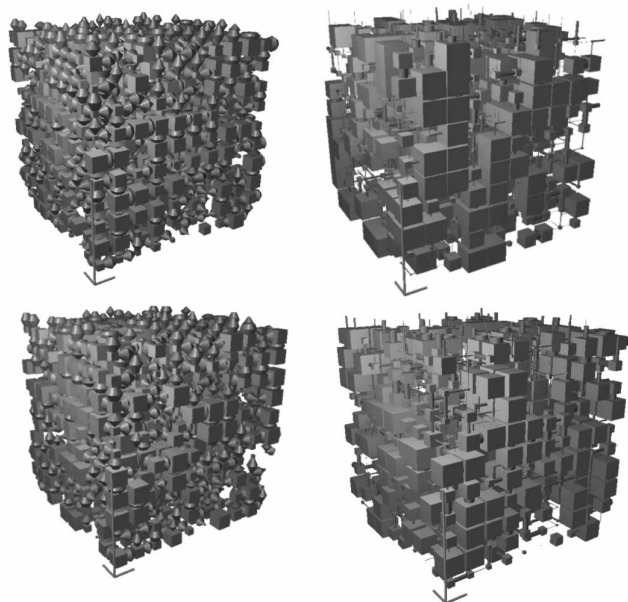


Fig. 9 Comparison of the unit cells with conical and cylindrical throats of structures 0.2634 fractional porosity (top row, unit cell side length 16.2 μm and 12.5 μm respectively) and 0.2704 fractional porosity (bottom row, unit cell side length 14.7 μm and 13.6 μm respectively).

5. Conclusions

A method has been presented which can be used to measure the permeability of porous materials. A hysteresis in permeability was observed performing an up-down sweep of driving pressure following apparent saturation by imbibition. Taking into account the effects of earlier discussed mechanisms of preferred pathway flow and film flow during imbibition, it is postulated that some pores remain unfilled after imbibition saturation such that there is entrapped air or vapour phase held in microscopic ganglia. This air may dissolve in polar liquids but does not dissolve in the aliphatic mineral oil used in the reported experiments. Even where millions of microscopic air bubbles would be trapped in the sample, they will not be detectable with the gravimetric possibilities offered by a modern microbalance. The values obtained from experimental permeability measurements, therefore, have to be evaluated within the boundary conditions of imbibition and the potential existence of preferential pathways.

The experimental permeability for the samples used in this study did not form a simple monotonic function of porosity. There is a local maximum permeability at a fractional porosity of ~ 0.26 . This local maximum is also clearly detected by the simulated network structures for these samples. Analysing the parameters of the computer network simulator it was found that there is no obvious discontinuity in any single parameter, rather, a combination of throat skew (throat size distribution) and connectivity is responsible. This supports a transition of some kind in the packing structure of the particulate material under different compressions. Permeability and porosity measurements could therefore readily be used to describe transitions in particle packing in compressed porous structures.

REFERENCES

1. C.J.Ridgway, J.Schoelkopf, P.A.C.Gane, accepted by Nordic Pulp and Paper Res. J. 18 (2003) 379.
2. G.P.Matthews, A.K.Moss, M.C.Spearing, F.Voland, Powder Technol. 76 (1993) 95.
3. R.Hilfer, Transport and Relaxation Phenomena in Porous Media, Wiley, New York, 1996.
4. H.Darcy, Les Fontaines Publiques de la Ville de Dijon, Dalmont, Paris, 1856.
5. P.C.Carman, Trans. of Inst. Chem. Eng. (Lond.), 15 (1937) 150.
6. J.van Brakel, Powder Technol. 11 (1975) 205.
7. F.A.L.Dullien, Porous Media: Fluid Transport and Pore Structure, Academic Press, Inc. New York, 1992.
8. S.Lohmander, M.Martinez, L.Lason, M.Rigdahl, Advanced Coating Fundamentals Symposium, Toronto, Tappi Press, Atlanta, 1999, p. 43.
9. S.Levine, P.Reed, G.Shutts, Powder Technol. 17 (1977) 163.
10. D.Seguin, A.Montillet, J.Comiti, F.Huet, Chem. Eng. Sci. 53 (1998) 3897.
11. D.Seguin, A.Montillet, J.Comiti, Chem. Eng. Sci. 53 (1998) 3751.
12. J.Schoelkopf, C.J.Ridgway, P.A.C.Gane, G.P.Matthews, D.C.Spielmann, J. Colloid Interface Sci. 227 (2000) 119.
13. C.J.Ridgway, K.Ridgway, G.P.Matthews, J. Pharm. Pharmacol. 49 (1997) 377.
14. D.M.W.Peat, G.P.Matthews, P.J.Worsfold, S.C.Jarvis, Eur. J. Soil Sci. 51 (2000) 65.
15. P.A.C.Gane, J.P.Kettle, G.P.Matthews, C.J.Ridgway, Ind. Eng. Chem. Res. 35 (1996) 1753.
16. G.P.Matthews, C.J.Ridgway, M.C.Spearing, J. Colloid Interface Sci. 171 (1995) 8.

17. C.J.Ridgway, P.A.C.Gane, *Colloids Surf. A: Physicochem. Eng. Aspects* 206 (2002) 217.
18. C.J.Ridgway, P.A.C.Gane, J.Schoelkopf, *J. Colloid Interface Sci.* 252 (2002) 373.
19. P.A.C.Gane, C.J.Ridgway, J.Schoelkopf, *Transp. Porous Media* 54 (2004) 79.
20. C.J.Ridgway, J.Schoelkopf, G.P.Matthews, P.A.C.Gane, P.W.James, *J. Colloid Interface Sci.* 239 (2001) 417.
21. C.H.Bosanquet, *Philos. Mag. S.6* 45 (1923) 525.
22. P.A.Bodurtha, G.P.Matthews, J.P.Kettle, S.Lohmander, P.W.James, in: *Proceedings of the Advanced Coating Fundamentals Symposium, San Diego, Tappi Press, Atlanta, 2001*, p. 393.
23. P.A.Bodurtha, G.P.Matthews, J.P.Kettle, I.Roy, accepted by *J. Colloid Interface Sci.* (2003).
24. M.A.Knackstedt, T.J.Senden, M.B.Lyne, in: *Proceedings of the Paper and Coating Chemistry Symposium, Stockholm, Sweden, 2000*.
25. P.A.C.Gane, J.Schoelkopf, D.C.Spielmann, G.P.Matthews, C.J.Ridgway, *Tappi J.* 83 (2000) 77.
26. J.Schoelkopf, PhD thesis, University of Plymouth, 2002.
27. J.Schoelkopf, P.A.C.Gane, C.J.Ridgway, D.C.Spielmann, G.P.Matthews, in: *Proceedings of the Tappi 2001 Advanced Coating Fundamentals Symposium, San Diego, Tappi, Atlanta, 2001*, p. 1.
28. D.C.Spielmann, personal communication, 2002.
29. R.M.German, *Particle Packing Characteristics*, Metal Powder Industries Federation, 1989.
30. M.Toivakka, K.Nyfors, *Tappi J.* 84 (2001) 49.